Dual-Band Shared-Aperture Dielectric Resonator Antenna (DRA) with Suppressed Cross-Band Interactions

Xing-Yu Cheng, *Student Member, IEEE,* Can Ding, *Senior Member, IEEE,* and Richard W. Ziolkowski, *Life Fellow, IEEE*

***Abstract*—As wireless technologies continue to advance, the collocation of diverse antennas operating at different frequency bands has become a common practice in various deployed communication platforms. However, antenna co-location introduces significant challenges, primarily in the form of substantial mutual interference among the antennas. In this paper, we explore the integration of two cylindrical dielectric resonator antennas (DRAs) operating at distinct frequency bands, specifically 3.5–3.9 GHz and 6.0–6.4 GHz, designed for uplink and downlink communication with satellites. These DRAs are nested concentrically, resulting in a dual-band shared-aperture DRA. However, the performance of this configuration is significantly compromised due to the interaction between the two DRAs. To mitigate these inteferences, two novel approaches are developed to suppress cross-band scattering and coupling, respectively. As a consequence, radiation patterns are restored and port isolations are improved. Subsequently, a prototype of the dual-band shared-aperture DRA was designed, fabricated, and tested. The measured results validate the effectiveness of these innovative interference mitigation techniques. The developed dual-band shared-aperture DRA represents a promising solution for installation on unmanned aerial vehicles (UAVs) to facilitate satellite communication.**

***Index Terms*—6G, cross-band decoupling, cross-band descattering, dielectric resonator antenna (DRA), dual-band, metasurface, shared-aperture antenna.**

I. Introduction

The advent of 6G network technologies promises significant advancements in wireless communication, offering expansive capacity and high-speed transmissions across a broad spectrum of frequencies. With the aim of fully harnessing the available frequency spectra, 6G is envisioned to extend its reach from terrestrial networks to encompass space networks, enabling three-dimensional (3D) coverage. This evolution towards 3D coverage is expected to foster deep integration and dynamic connectivity among multiple systems [1]. Within this paradigm, unmanned aerial vehicles (UAVs) can play a critical role in a space-air-ground integrated network by facilitating the interconnections of satellite communications, terrestrial communications, and communications via drone swarms [2], [3], [4]. Therefore, multiple antenna systems are commonly incorporated in UAVs to fulfill various functionalities and communication needs. However, they should be fully integrated to minimize their weight and the amount of space they occupy.

One efficient approach to achieve this integration is through the implementation of a shared-aperture configuration, which can be realized with various techniques. These include interleaved [5], [6], embedded [7], [8], [9], and stacked [10], [11], [12] schemes. However, the close proximity of two antennas, especially when employing a shared-aperture configuration, increases the risk of cross-band interactions between them. Cross-band interactions can be classified technically into two types: mutual coupling and scattering [13]. Mutual coupling is generally associated with the degradation of port isolation, whereas scattering typically leads to the distortion of radiation patterns. Either of them poses significant risks to signal quality in a communication system.

Cross-band interaction has garnered significant attention in recent years, particularly in base station antenna arrays. The latter often collocate dual-band antennas in a compact platform. Several methods have been proposed to address the associated degradation in their radiation patterns and/or their port isolations [14], [15], [16], [17], [18], [19], [20]. For example, additional filtering techniques were employed for both the LB and HB antennas in [14]. They included the use of 2.5-dimensional cloaks, defected ground structures, and resonance shifters. The inherent filtering response of LB elements was employed in [14], [15], [16] to significantly suppress cross-band mutual coupling and scattering among those closely spaced elements. Another approach has introduced chokes [17], [18], [19]. For instance, spiral chokes were integrated into a dual-band 4G and 5G array to reduce cross-band scattering and enhance the bandwidth of the choked element [17]. The conductors of the LB elements in [18] were divided into shorter sections by incorporating chokes, significantly reducing the currents induced by HB radiation. Furthermore, metasurfaces have also been adopted to alleviate undesirable scattering effects [16], [20]. For example, a low-pass grid frequency selective surface (FSS) was designed in [20] to suppress the cross-band mutual coupling. The FSS's minimal scattering feature efficiently reduced the port coupling from -14 to -35 dB without compromising its radiated field performance in the high band.

Dielectric resonator antennas (DRAs) have been employed extensively across various fields for several decades. Their per-

Manuscript submitted November 20, 2023; revised February 08, 2024. This work was funded by Australian Research Council (ARC) DECRA under grant DE200101347. *(Corresponding author: Can Ding.)*

Xing-Yu Cheng and Can Ding are with the Global Big Data Technologies Centre, University of Technology Sydney (UTS), NSW 2007, Australia (e-mail: Xingyu.Cheng@student.uts.edu.au; can.ding@uts.edu.au).

R. W. Ziolkowski is with the University of Arizona, Tucson AZ 85721, USA (E-mail: ziolkows@arizona.edu).

formance characteristics, which encompass high efficiencies, wide bandwidths, and ease of excitation, are very attractive for many applications [21]. Moreover, DRAs offer additional advantages when compared to other antenna types such as preserving degrees of freedom in multiple dimensions and exhibiting low losses, especially at high frequencies. As a result, DRAs are considered to be an ideal choice for numerous present and future wireless communication systems, including those deployed on UAVs [22]. Research on in-band decoupling of DRAs has also been ongoing for years. Techniques to mitigate port isolation have included using metamaterial-based isolation walls [23], [24]; electromagnetic bandgap (EBG) structures [25]; FSSs [26]; conformal microstrips lines [27], [28]; and placing metallic vias inside a DRA element [29]. Recently, self-decoupling methods without any extra structures have been proposed [30], [31], [32]. Nevertheless, these reported research efforts only consider DRAs in the same frequency band. There has been no research to date that focuses on suppressing cross-band interactions between DRAs operating in two different frequency bands in a shared aperture configuration.

In this paper, suppression of the mutual coupling and scattering between two cylindrical DRAs in a shared-aperture configuration is achieved for the first time. The two cylindrical DRAs are nested concentrically and operate in two distinct frequency bands that cover the C-band uplink and downlink for communication between UAVs and satellites. This layout minimizes the space utilized, a key consideration for antennas on a drone. To address the cross-band interaction between the high-band (HB) element and the low-band (LB) element, as well as the effects from the feed structure, a conformal semi-transmissive metasurface is inserted between the two elements. It modifies the HB field distribution and facilitates the restoration of the HB radiation patterns. C-shaped slots and tuning fork microstrip feedlines are introduced in order to enhance the port isolation in the low band while feeding the HB element. A prototype of the optimized dual-band shared-aperture DRA system was fabricated and measured. The experimental results, in agreement with their simulated values, confirm both the anticipated isolation and pattern enhancements.

This paper is organized as follows. The dual-band shared-aperture DRA configuration is detailed in Section II. Its simulated radiation characteristics are presented along with the main parameter studies of the metasurface introduced into its structure to restore the high-quality patterns associated with each band. The operating principles of a new feed structure consisting of two C-shaped slots and a fork tuning feed line, which is introduced to reduce the cross-band coupling, are described in Section III. Its impact on radiation characteristics is also demonstrated. Fabrication and testing of the final share-aperture DRA prototype are described in Section IV. Finally, the conclusion is presented in Section V, followed by acknowledgments in Section VI.

All of the presented results were obtained using the commercial software package AnsysEM22.1, i.e., the ANSYS high frequency structure simulator (HFSS). These HFSS models took into account the realistic properties of every material present in them. Consequently, because they are full-wave finite-element-based simulations, they implicitly accounted for all mutual coupling and scattering effects, as well as all loss mechanisms.

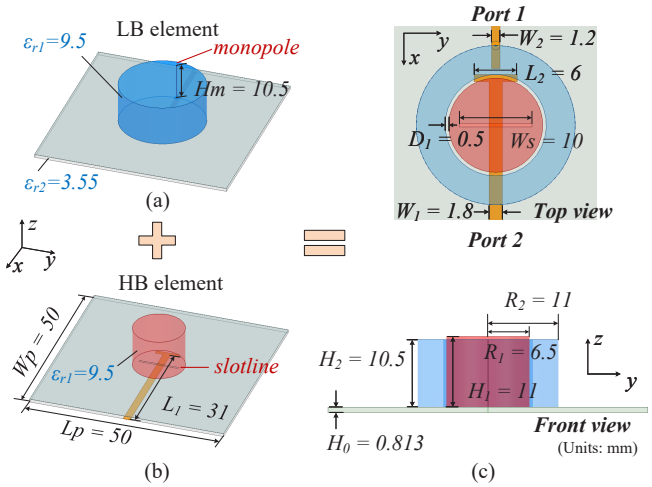

Fig. 1. Components of the dual-band DRA. (a) LB cylindrical DRA. (b) HB cylindrical DRA. (c) Top view and front view of these DRAs in their shared-aperture configuration.

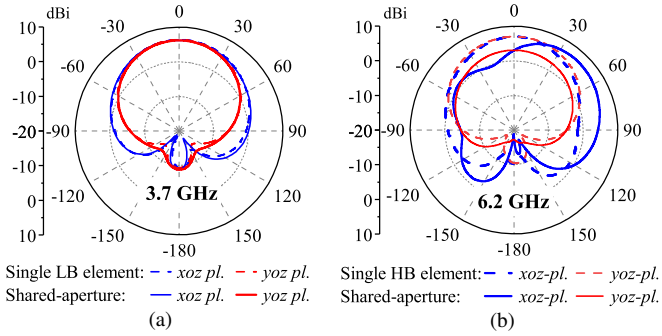

Fig. 2. Comparison of gain patterns of the individual elements and in the shared-aperture configuration. (a) LB element at 3.7 GHz. (b) HB element at 6.2 GHz.

II. Cross-Band Scattering Suppression

A. Dual-Band Shared-Aperture DRAs

As depicted in Figs. 1(a) and (b), two cylindrical DRAs are placed individually on the same planar square copper-cladded substrate (ε_{r2} = 3.55). Each has a dielectric constant of 9.5. The LB element is excited by a monopole and is fed by a microstrip line etched on the bottom surface of the substrate. The HB element is excited by a slot in the top surface of the substrate that is fed by a T-shaped microstrip line etched on its bottom surface. These initial LB and HB DRAs operate in their $HEM_{11\delta}$ mode around 3.7 and 6.2 GHz, respectively. They are broadside-radiating.

A shared-aperture configuration was employed to seamlessly combine the two elements. It diverges from the conventional side-by-side placement which requires an impractically large area on a mobile platform like a small drone. As depicted in Fig. 1(c), the HB element is positioned concentrically within the LB element with an air gap having a thickness of D_1.

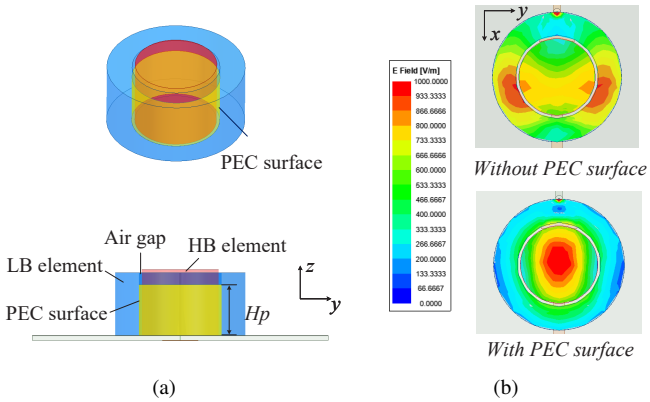

Fig. 3. Shared-aperture DRAs isolated by an ideal conformal PEC surface. (a) Configuration with a PEC surface between the LB and HB elements. (b) E-field distributions with and without the PEC surface at 6.2 GHz.

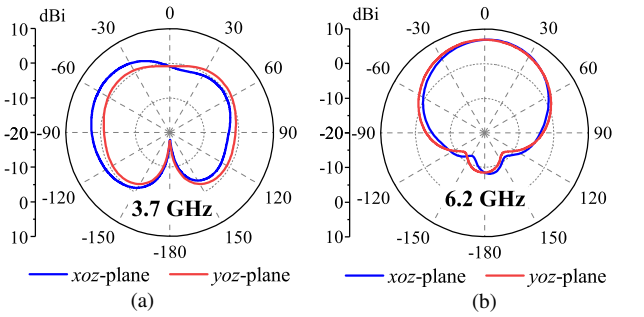

Fig. 4. Gain patterns with the PEC surface present. (a) LB element at 3.7 GHz. (b) HB element at 6.2 GHz.

This configuration enables a tightly integrated arrangement without the requirement of extra feeding structures. However, the shared-aperture configuration poses new challenges. The simulated gain patterns of the individual and share-apertured DRAs are shown in Fig. 2. Comparing the independent and shared-aperture LB results, the patterns remain approximately the same. On the other hand, noticeable distortions of the shared-aperture HB pattern occur in the *xoz*-plane and a gain decrease from 6.8 to 3.3 dBi occurs in the *yoz*-plane. These effects were found to be caused by the influence of higher order modes excited in the surrounding dielectrics and the presence of the feeding monopole in the LB element.

B. Working Mechanisms of the Descattering Approach

To address this problem, an infinitesimally thin PEC surface with a height *Hp* was affixed to the inner surface of the LB element and separated from the HB element by a minimal 0.5 mm gap, as shown in Fig. 3(a). Fig. 3(b) illustrates the electric field (E-field) distribution with and without the PEC surface being present when the HB element is excited at 6.2 GHz. It is found that without the PEC surface, the E-field is symmetric with respect to the *x*-axis but is noticeably not concentrated in the HB element. Thus, the $\mathrm{HEM}_{11\delta}$ mode of the HB element alone is severely disrupted in the shared-aperture configuration. A conformal PEC surface, slightly lower than the DRAs (*Hp* = 6.5 mm), facilitates the restoration of the original mode. While complete field isolation is not attained, a majority of the E-field is nevertheless concentrated about the center of the HB element.

The simulated gain patterns with the PEC surface present are given in Fig. 4. Fig. 4(a) illustrates that the HB patterns in both principal planes are effectively restored to those of the HB DRA alone. However, as depicted in Fig. 4(b), the introduction of the PEC surface has an impact on the LB patterns. This occurs because the PEC surface blocks the fields radiated by the monopole from entering into the HB element. Consequently, a metasurface was designed to enable the penetration of the LB fields into the HB element while preventing the penetration of HB fields into the LB element.

C. Conformal Semi-Transmissive Metasurface Design

The design of this metasurface was challenging because of three issues. First, the distance between the LB and HB elements is a mere 0.5 mm. Consequently, careful attention to the near-field characteristics of the metasurface was essential. Second, the metasurface must be conformal to a cylinder. Third and most important, it was essential for the metasurface to not entirely block the penetration of the HB fields into the LB element. In fact, it was crucial for it to allow a portion of the HB fields to pass through. This feature replicates the scenario when the HB DRA operates by itself. It is essential because a fraction of the HB fields can escape the dielectric material in such soft boundary cases. In contrast, a hard boundary would act like a metal cavity. Consequently, the metasurface must facilitate high transmission for the LB fields and partial blocking of the HB fields, a characteristic that we refer to as "semi-transmissive".

To optimize the metasurface's design and ensure its accuracy, HFSS simulations were performed following these steps:

(1) Simulation of the unit cell's initial design as a planar element and its response to a normally-incident plane wave.

(2) Optimization of the filter response of the conformal half-ring metasurface alone with the radius of its exterior dielectric wall equal to the inner radius of the LB annular cylinder.

(3) Simulation of the dual-band shared-aperture configuration with the semi-transmissive metasurface being present.

(4) Iterate until the desired performance characteristics are achieved.

The first step mimics a plane wave field normally incident on an infinite planar metasurface. The unit cell of the metasurface was designed in HFSS with the waveguide model depicted in Fig. 5(a). Its side walls employed Master-Slave boundary conditions to establish periodic behavior in the *x* and *y* directions. The top and bottom surfaces were taken to be Floquet ports to launch the incident field and receive the reflected and transmitted fields. The unit cell consists of a square copper loop printed on a thin square dielectric sheet of side length *Ld* = 5.85 mm. The loop's exterior side-length is *La* = *Wa* = 5.6 mm; the width of its traces is T_1 = T_2 = 0.25 mm; and the thickness of copper is 0.018 mm. Taking into account the desired conformal configuration, a flexible material with a relative permittivity ε_{r3} = 3.4 and a loss tangent of 0.004 is introduced; its thickness is *Hf* = 0.0508 mm. Two square dielectric blocks are positioned above and

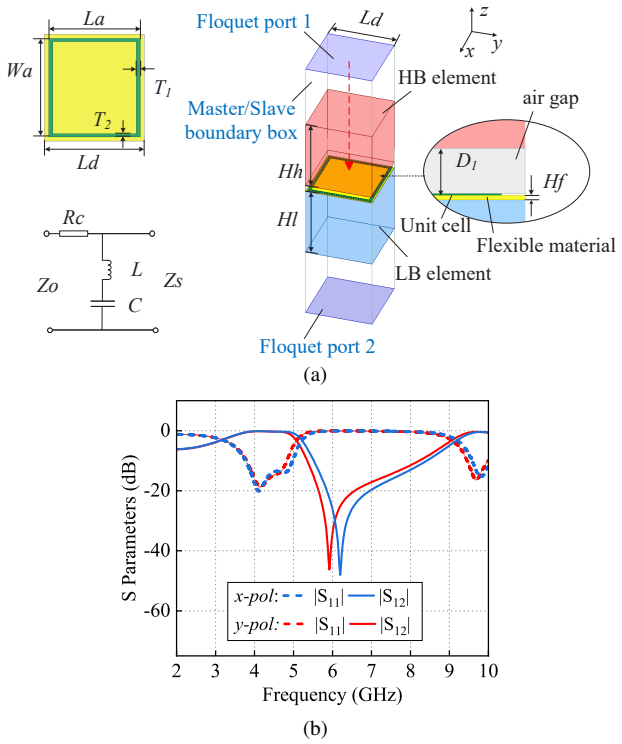

Fig. 5. Design of the metasurface with its dimensions labeled. (a) The inclusion in its unit cell is a square loop of copper printed on the top of a thin square flexible material. The unit cell was simulated with the illustrated HFSS model. The bottom of the sheet is attached to the inner wall of the LB element (blue region) with the loop in the air gap between the HB element (red region). The equivalent circuit of the unit cell is also illustrated. (b) Simulated frequency response of the metasurface when a plane wave was normally incident on it.

below the unit cell. They represent the LB (blue) and HB (red) elements, respectively. Their heights are $Hl = Hh = 6.0$ mm. The thickness of the air gap between these two blocks is $D_1 = 0.5$ mm. Its equivalent LRC circuit model representing a band-stop filter is also shown in Fig. 5(a).

The metasurface's simulated responses in reflection and transmission are shown in Fig. 5(b). For both *x*-polarized and *y*-polarized waves, these results indicate that the metasurface exhibits a good reflection response from 5.3–8.2 GHz and a good transmission response from 3.7–4.9 GHz. However, the size of this unit cell is not appropriate to achieve a ring metasurface conformal to the LB annular dielectric in the near field.

The second and third steps provided the means to design an appropriate conformal ring metasurface. As illustrated in Fig. 6(a), half of the structure was simulated to reduce the computational requirements. The unit cells on the corresponding metasurface half-ring conformed to the inner surface of the LB DRA, which was not physically present in the simulations. The E-fields excited within the HB DRA are mostly vertically polarized. Consequently, the HFSS model was configured to excite a vertically-polarized E-field. The top and bottom *xy*-surfaces were taken to be perfect electric conductors (PECs), while the simulation region surfaces orthogonal to the *y*-axis were taken to be perfect magnetic conductors (PMCs). Thus, the model has infinite periodicity in the *y*- and *z*-directions.

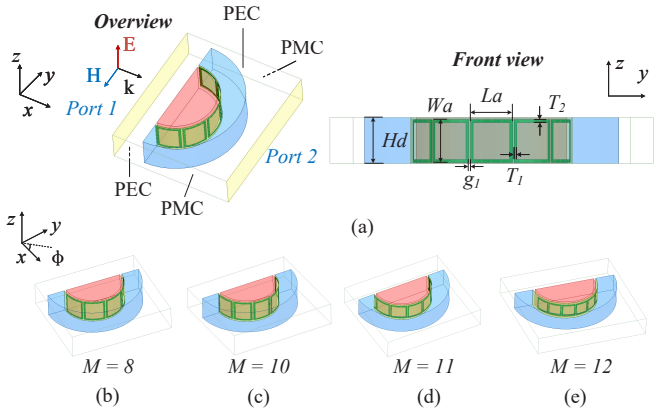

Fig. 6. Conformal half-ring metasurface unit cell configuration. (a) HFSS model (with the indicated boundary conditions the structure is repeated along the *y*-and *z*-directions out to infinity). Varying numbers of unit cells (b) M = 8; (c) M = 10; (d) M = 11; (e) M = 12.

TABLE I
PARAMETERS OF THE CONFORMAL RING METASURFACE (UNITS: MM)

Number of unit in full ring	*La*	*Wa*	T_1	T_2	*Hd*	g_1
M=8	4.8	5	0.35	0.35	5.5	0.3
M=10	4.1	4.5	0.4	0.3	5.1	0.3
M=11	3.8	4.1	0.25	0.4	5.0	0.2
M=12	2.8	3	0.2	0.35	4.2	0.2

Port1 and Port2 were introduced as the surfaces orthogonal to the *x*-axis and launched the desired vertically-polarized E-field. Thus, the periodicity along *z* had no impact on the results; the distances of the sidewalls from the structure were adjusted to ensure that they had no impact as well. The model facilitates obtaining the reflection from and transmission through the metasurface with the HB DRA being present. Although differences remain with the actual physical structure, it offers essential guidance for the optimization of the initial parameters. Note that the actual material used in the prototype had to be flexible so that it could be printed in a planar format and then shaped into a ring during assembly of the shared-aperture system.

To achieve the desired filter response, the size and number of unit cells in the azimuthal direction that defined the ring structure had to be adjusted. A rectangular ring unit cell was found to be the most convenient, especially for fabrication purposes. A planar portrait (*yoz*-plane) of the ring structure and its design parameters are shown in Fig. 6(a). The horizontal (*y*-axis) and vertical (*z*-axis) lengths are denoted as *La* and *Wa*, respectively. The widths of the corresponding traces are denoted as T_2 and T_1. Setting M as the number of unit cells that fit within the perimeter of the entire ring, we focused on four cases: M = 8, 10, 11, 12. They are illustrated in Figs. 6(b)-(e). The detailed values for each M are listed in Table I.

Their simulated transmission responses are displayed in Fig. 7. When M = 8, 10, 11, and 12, the transmission null is at 5.8, 6.0, 6.2, and 6.4 GHz, respectively. On the other hand, their insertion losses were approximately 5 dB within the low band (3.5–4.0 GHz). Our final selection, M = 11, was chosen

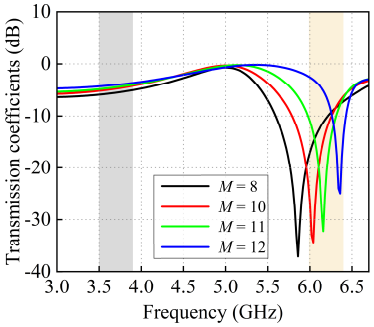

Fig. 7. Transmission coefficients of the conformal ring metasurface for different numbers (M) of unit cells along its perimeter.

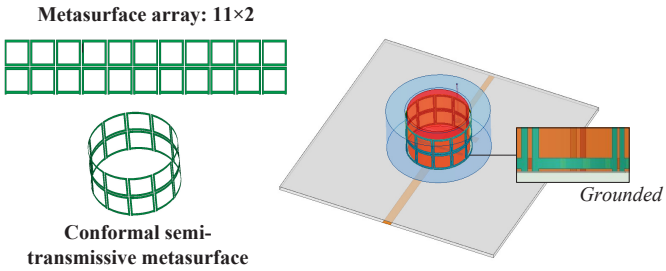

Fig. 8. Configuration of shared-aperture system with the optimized conformal ring metasurface present.

to achieve the desired filtering response with a transmission null centered in the HB within the range of 6.0 to 6.4 GHz. It was critical that the transmission coefficient of the ring metasurface was not as small as it would be with a PEC wall or even typical FSS structures. It was intentionally designed to be semi-transmissive, i.e., only around -7 dB at 6.4 GHz.

A finite height metasurface was required for the actual shared-aperture system. It was determined that a ring metasurface with the selected $M = 11$ unit cells along its perimeter and with 2 unit cells in its z-direction is appropriate for the heights of the LB and HB dielectrics. This conformal semi-transmissive ring metasurface is depicted in Fig. 8. Note that its height is lower than either DRA, which also guarantees that it does not fully obstruct the HB radiation, further assuring its semi-transmissive nature. The detailed inset indicates that each of the unit cells in its lower row was connected to the ground with a short stub. The reason for its presence is illustrated by the simulation results in Fig. 9.

When the metasurface was not grounded, as depicted in Fig. 9(a), strong coupling between the metasurface and the ground plane occurred within the HB range. It resulted in radiation leakage along the horizontal ground plane, which introduced distortions into the radiation patterns. In contrast, when it was appropriately grounded, the coupling to the ground plane is markedly diminished, which ensures its effectiveness in restoring the original radiation patterns. Note that the vertical side of each stub was extended by 0.1 mm to facilitate the subsequent assembly of the system. The final dimensions of the ring structure were optimized numerically; they are detailed in Table II.

The electric field vector distributions at 6.2 GHz for 3

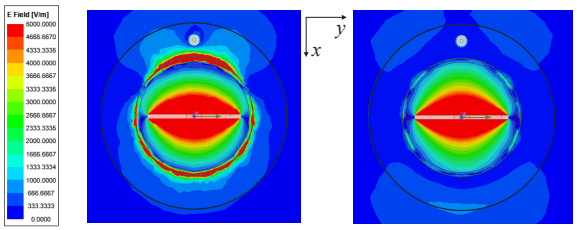

Fig. 9. Electric field distribution on the ground plane when the HB element is excited at 6.2 GHz. (a) Semi-transmissive metasurface not grounded. (b) Semi-transmissive metasurface grounded.

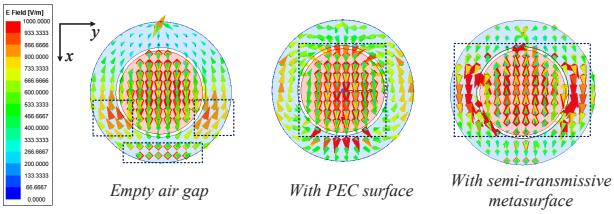

Fig. 10. Electric field vector distribution when the HB element is excited at 6.2 GHz for three different cases.

cases are compared in Fig. 10: air gap alone, PEC surface in the air gap, and the conformal ring metasurface in the air gap and attached to the LB element. The dotted regions highlight particular vector behaviors. Compared to case 1 in which no descattering structure is present, the PEC structure in case 2 concentrates the E-field into the center of the HB dielectric. Case 3 achieves a similar effect without requiring a full shielding of the induced scattering. This intended semi-transmissive property effectively enhances the radiated fields.

Fig. 11 plots the gain patterns of the HB element and LB element before and after the ring metasurface is present. One observes that despite the gain drop from 6.3 to 5.4 dBi at 3.9 GHz, the overall performance of LB element is not greatly affected. On the other hand, a significant improvement in the HB performance has been achieved as illustrated in Fig. 11. The tilting and distortions of the patterns in the xoz-plane have been greatly suppressed. Moreover, the co-polarization gain in the yoz-plane increases from 3.4 to over 6.6 dBi. These results demonstrate the effectiveness of the ring metasurface as a useful descattering tool that facilitates the LB and HB elements radiating without interfering with each other in the shared-aperture configuration.

Fig. 12 presents a Smith chart comparison of the impedance matching realized for three configurations: the single LB/HB DRA (case m1), the dual-band shared-aperture DRA without

TABLE II
PARAMETERS OF THE OPTIMIZED CONFORMAL SEMI-TRANSMISSIVE METASURFACE (UNITS: MM))

Parameters	***Hm***	L_1	***Lp***	***Wp***	L_2	W_2	D_1	***Ws***	W_1	H_2
Value	10.5	30.3	50	50	12	1.2	0.5	11	1.8	10.5
Parameters	R_2	R_1	H_0	H_1	***La***	***Wa***	T_1	T_2	g_1	g_2
Value	11	6.5	0.813	11	3.8	4.1	0.25	0.4	0.15	0.16

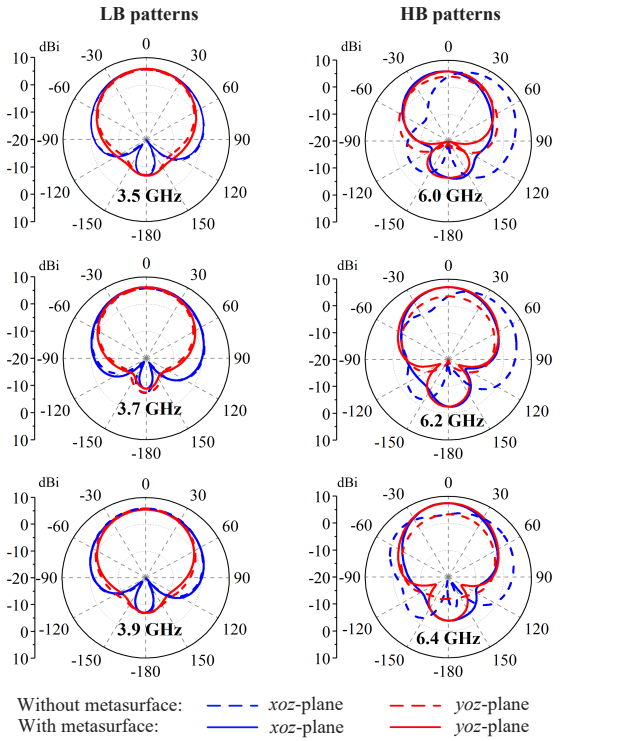

Fig. 11. Gain patterns of the shared-aperture system with the conformal semi-transmissive ring metasurface present in the LB and HB frequencies.

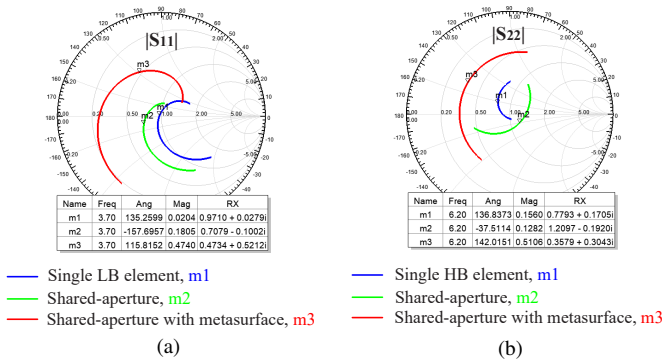

Fig. 12. Smith chart representation of the impedance matching for three different configurations, Case m1-m3, at center frequency of each case (a) LB (3.5–3.9 GHz). (b) HB (6.0–6.4 GHz).

the metasurface (case m2), and the dual-band shared-aperture DRA equipped with a metasurface (case m3). Each one is fed by the same original straight slot or monopole. Fig. 12(a) illustrates that when the HB DRA is placed within the LB DRA, there is only a minor alteration in the input impedance of the LB DRA. While the introduction of the metasurface also induces changes in the input impedance, they follow a trend similar to the original one. Conversely, Fig. 12(b) shows that the collocation of the HB and LB DRAs notably modifies the input impedance of the HB DRA. The associated changes are quite evident in the distinct blue and green curves. The input impedance exhibits a variation trend again similar to the original one after the metasurface is introduced. However, the red curve's variation range is larger than that of the blue curve, which indicates an increased impedance matching complexity. In summary, while the metasurface does influence the impedance matching, the impact is not substantial. Impedance matching is still achieved by optimizing the feed network, albeit with only a slightly reduced bandwidth.

Unlike conventional FSS designs [11], [20] employed for base station antennas to mitigate cross-band scattering, our metasurface is tailored to the unique challenges encountered within the shared-aperture DRA configuration. A conformal structure is adopted that adheres to the outer cylindrical surface of the HB DRA and is separated from the inner cylindrical surface of the LB DRA by a negligible distance. This arrangement is a far more intricate and, hence, demanding to realize in comparison to existing planar FSS designs. Moreover, our metasurface boasts a significantly smaller size, being compactly integrated into the system. Our approach deviates significantly in this manner from the large-aperture FSSs employed in conventional methods. Furthermore, by minimizing the distance from the metasurface to the HB radiator, the configuration effectively addresses issues related to proximity and coupling. Finally, while the conventional FSS approach aims to completely block radiation from either the LB or HB element, our metasurface is innovatively designed to only "partially block" the HB radiation. The outcome is a distinctive and highly effective approach to mitigate cross-band interactions in any shared-aperture DRA system.

III. Cross-band Isolation Enhancement

The input reactance of the original dual-band shared-aperture DRA design was greatly increased when the metasurface was present. The height of the HB element was increased to H_1 = 15.0 mm to compensate for its presence to achieve impedance matching. Fig. 13 displays the resulting simulated S-parameters. Unfortunately, the port isolation values, i.e., $|S_{12}|$ in the two operating bands, is negatively impacted due to the cross-band coupling. As shown in Fig. 13(a) and 13(b), the minimum port isolation is only 5.9 and 13.6 dB in the LB and HB, respectively.

To address this problem, the slot and its feedline were redesigned. Their evolution to the final design is illustrated in Fig. 14. The original straight slot and its T-shaped feed line (Configuration 1) are shown in Fig. 14(a). It was first modified to the C-shaped rectangular slot excited by a short tuning fork feedline (Configuration 2) as shown in Fig. 14(b). The short sides of the rectangle are along the x-axis. This configuration was further modified into Configuration 3, shown in Fig. 14(c), by introducing a second C-shaped slot that mirrors the first one with respect to the y-axis. These two slots are excited by a longer tuning fork feedline. The overall structure is symmetric, i.e., the slots are mirror-symmetric with respect to the y-axis and the stems of the tuning fork feedline are symmetric with respect to the x-axis.

Figs. 15(a), 15(b), and 15(c) depict the magnetic current distribution and E-field distribution near the slots in Configurations 1, Configuration 2, and Configuration 3 respectively, at both LB (3.6 GHz) and HB (6.1 GHz) frequencies. Note that these slots are designed to feed the HB element. At the HB frequency, the straight slot functions as a half-wavelength magnetic dipole, whereas the C-shaped slots operate as a

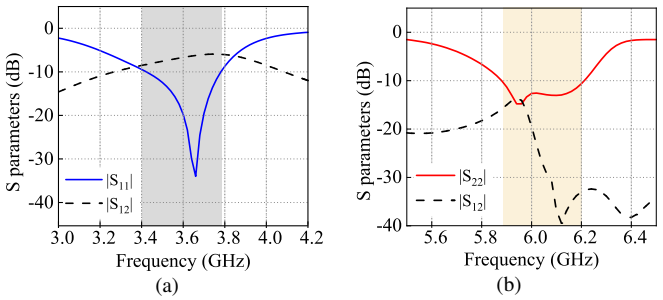

Fig. 13. Simulated S-parameters of the dual-band shared-aperture DRA with the conformal semi-transmissive ring metasurface is present. (a) LB. (b) HB.

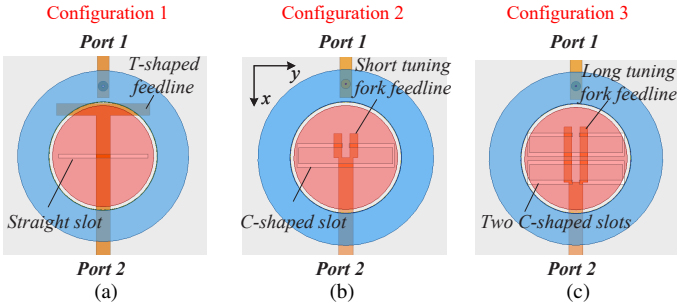

Fig. 14. Dual-band shared-aperture DRA configuration with its HB element excited with three different slot structures and their feed lines. (a) Configuration 1. (b) Configuration 2. (c) Configuration 3.

folded magnetic dipole. This description is confirmed by the E-field distribution in Fig. 15. Both the straight slot and the C-shaped slots effectively excite the DRA at the HB frequency.

The primary differentiation between the straight and the C-shaped slots becomes evident at the LB frequency. As depicted in Fig. 15(a), the straight slot retains its ability to effectively excite the DRA, despite its length being shorter than half a wavelength at the LB frequency. This leads to a pronounced coupling between the LB and HB ports. In contrast, the C-shaped slot in Fig. 15(b), which measures approximately one wavelength at the LB frequency, can be visualized as a rectangular folding of the straight slot. The opposing current orientation along the y-axis within the C-shaped slot results in a significant reduction in emissions at the LB frequencies. Thus, a considerable improvement in the isolation between the LB and HB ports is achieved. As shown in Fig. 15(c), the mirror symmetry-based C-shaped slots exhibit behavior akin to the single C-shaped slot but effectively mitigate the asymmetries, resulting in a more symmetric radiation pattern and decreased cross-polarization levels.

Fig. 16 compares the simulated $|S_{11}|$ and $|S_{12}|$ values over the LB for these three slot configurations when the HB element is excited. As indicated by blue and red dashed lines, the port isolation $|S_{12}|$ values in Configurations 2 and 3 have increased remarkably to over 25 dB in comparison to those in Configuration 1. In fact, the maximum isolation reaches up to 40 dB within that band. Therefore, very good LB port isolation is obtained. Note that the substitution of the C-shaped slot for the straight one has the effect of shifting the impedance matching band of the LB port to higher frequencies. This shift

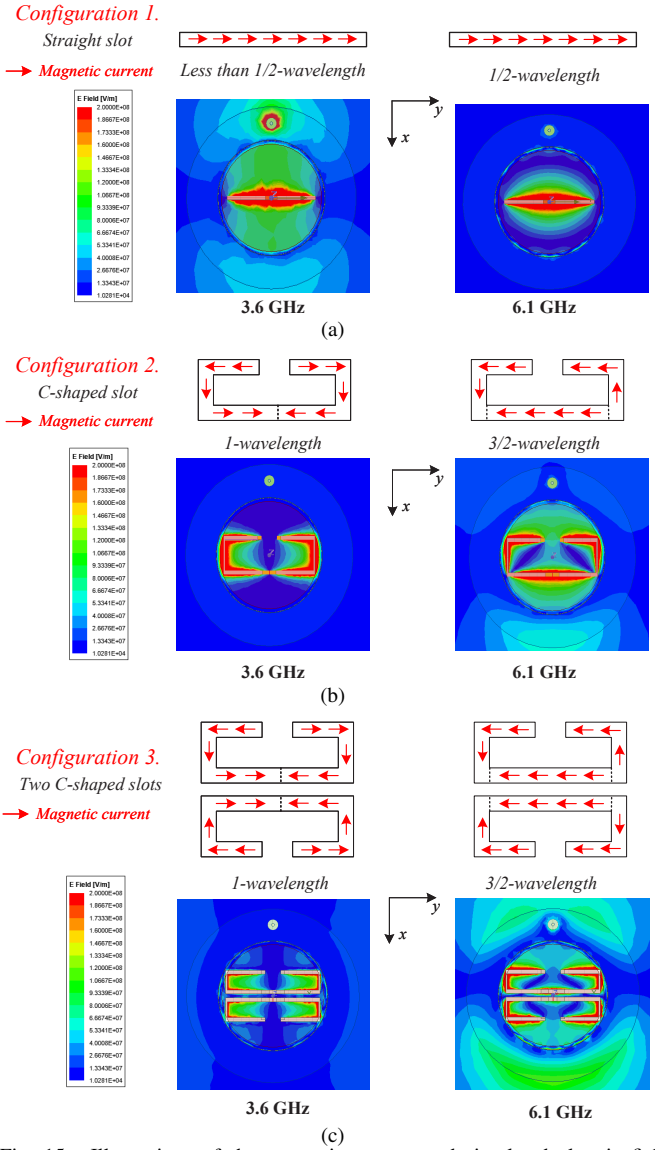

Fig. 15. Illustrations of the magnetic current and simulated electric field distributions near the slot(s) at 3.6 GHz and 6.1 GHz. (a) Configuration 1: straight slot. (b) Configuration 2: C-shaped slot. (c) Configuration 3: Two C-shaped slots.

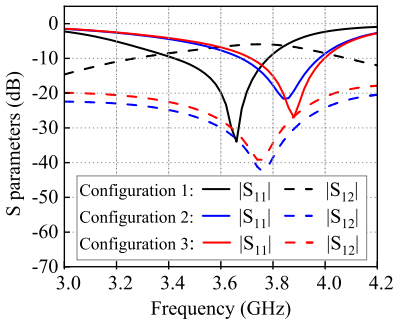

Fig. 16. Simulated $|S_{11}|$ and $|S_{12}|$ values of the dual-band shared-aperture DRAs in the LB as functions of the source frequency for the three feed configurations shown in Fig. 14.

occurs even though the slots are not utilized to excite the LB. Nevertheless, the desired $|S_{11}|$ bandwidth is attained simply by making adjustments to the dimensions of the feed structure.

When Configuration 3 was adopted, the impedance match-

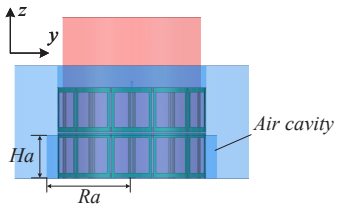

Fig. 17. Front view of the dual-band shared-aperture DRA in configuration 3, with a ring air cavity introduced inside LB element.

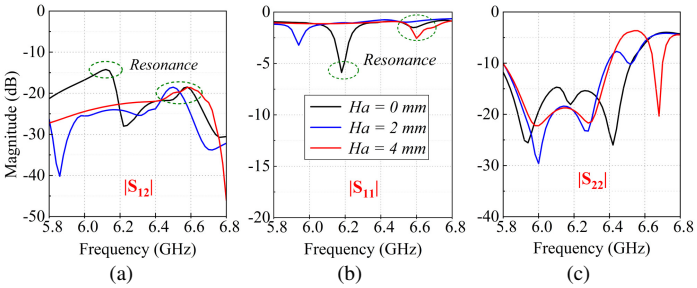

Fig. 18. Simulated S-parameters for different air cavity heights. (a) $|S_{12}|$ curves. (b) $|S_{11}|$ curves.(c) $|S_{22}|$ curves.

ing and isolation in the HB were also affected. This issue was addressed by etching additional dielectric from the LB DRA to create a ring air cavity. This configuration is depicted in Fig. 17. The air cavity is concentric with the LB element and is located within its lower portion. Its height is Ha = 4 mm, and it has an edge-to-center distance Ra = 8.0 mm. The simulated transmission coefficient and reflection coefficient values are displayed in Fig. 18 with and without the presence of the air cavity for various air cavity heights. As seen in Fig. 18(a), an undesired resonance occurs in the $|S_{12}|$ values at around 6.15 GHz when the air cavity is absent. It leads to a noticeable decrease in the port isolation. Simultaneously, a resonance in the $|S_{11}|$ values is evident in Fig. 18(b) at the same frequency. It indicates that the LB DRA unexpectedly resonates in the HB at 6.15 GHz despite it having been designed specifically for the lower frequencies. Introducing the air cavity outside the HB DRA alters the equivalent size of the LB DRA. As shown in Fig. 18(b), the resonance in the $|S_{11}|$ values shifts to higher frequencies as the air cavity height increases. This behaviour facilitates moving the resonance in the $|S_{12}|$ values out of the HB without impacting the impedance bandwidth of the HB DRA as the air cavity height changes.

Additionally, the radiation patterns undergo changes depending on the height of the air cavity. As depicted in Fig. 19, there is a noticeable disparity in the beamwidths between the *xoz* and *yoz* planes for the shorter air cavity with Ha = 2.0 mm. It arises from the unwanted resonance being shifted to 6.5 GHz, which is still close to the upper limit (6.4 GHz) of the targeted HB band. This effect negatively impacts the desired recovery of the independence of the two radiators. Consequently, the taller air cavity with Ha = 4.0 mm was chosen. The resulting radiation patterns closely resemble those produced by the corresponding single HB element when it is operated independently. Fig. 20 illustrates the electric field distribution within the LB and HB in the final configuration.

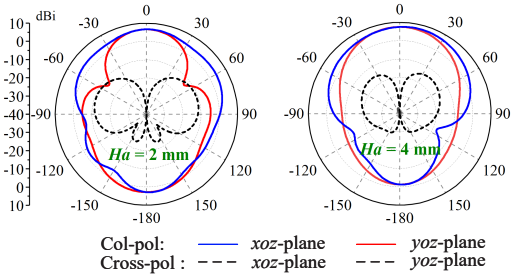

Fig. 19. Gain patterns of the HB DRA at 6.4 GHz for different heights of the air cavity.

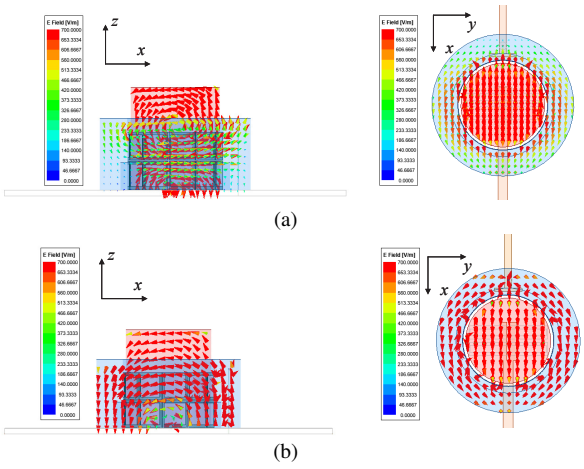

Fig. 20. Electric field distribution of the shared-aperture DRA in its final configuration. (a) LB element at 3.7 GHz. (b) HB element at 6.2 GHz.

TABLE III
PARAMETERS OF THE OPTIMIZED DUAL-BAND SHARED-APERTURE DRA (UNITS: MM)

Parameters	W_1	W_2	L_3	W_3	L_4	L_5	L_6	H_1	H_2	Ha	R_1
Value	1.5	1.1	5.8	1	22	17	4.2	15	10.5	4	6.5
Parameters	***Hm***	***dm***	***Ra***	Ls_1	Ls_2	Ls_3	Ws_1	Ws_2	g_3	g_4	R_2
Value	9.8	15.8	8	12	2	5.9	0.5	0.15	0.2	0.5	11

It is evident from these vector field plots that the LB element remains operating in its $HEM_{11\delta}$ mode, consistent with the mode of the original single LB DRA. However, the HB DRA shifts its operation to the $HEM_{11\delta+2}$ mode. This change occurs because of the increase in its height in comparison to the original configuration.

The final configuration of the designed dual-band shared-aperture DRA is shown in Fig. 21. Note that several design enhancements were introduced that take its assembly into consideration. First, four dielectric location dowels were integrated into the DRAs, two for each element. They ensure that they are in a concentric arrangement after assembly. Second, there are eleven via holes drilled into the substrate in order to have the tabs of the conformal metasurface be securely inserted into them and then fastened to the ground plane to ensure its proper grounding. These supplementary structures were included into the HFSS model, and it was confirmed that they have no adverse effects on the desired performance outcomes. Fig. 21(b) clearly shows the physical configuration

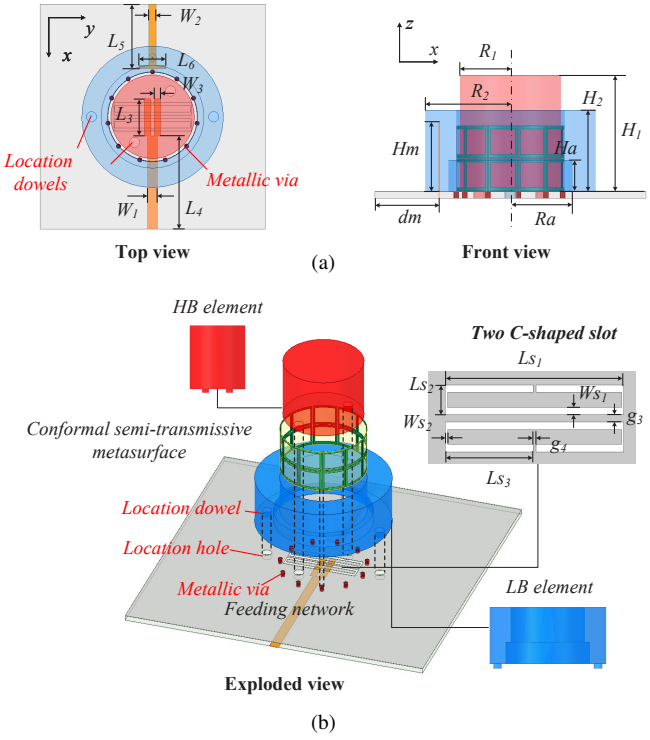

Fig. 21. Final configuration of the developed dual-band shared-aperture DRA. (a) Top view and front view. (b) Exploded view.

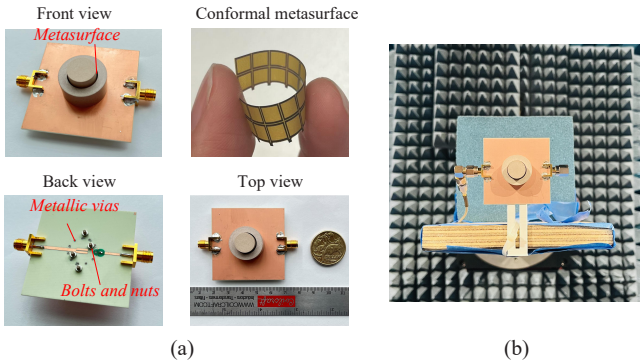

Fig. 22. Photos of the dual-band shared-aperture DRA prototype. (a) Views of the components before and after their assembly. (b) Assembled antenna in the measurement chamber.

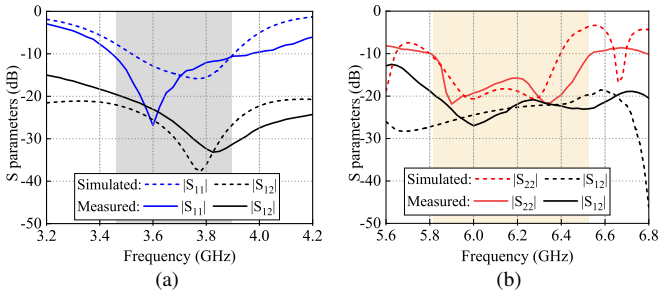

Fig. 23. Simulated and measured reflection and transmission coefficients of the dual-band shared-aperture DRA. (a) LB. (b) HB.

in an exploded view. color/redThe parameters of the optimized dual-band shared-aperture DRA are given in Table III.

IV. Experimental Results

A prototype of the optimized dual-band shared-aperture DRA was fabricated, assembled, and measured to verify the suppressed cross-band interactions. It is shown in Fig. 22. The DRAs were fabricated with a composite ceramic (relative permittivity $\varepsilon_{r1} = 9.5$, loss tangent $\tan\delta = 0.0029$). The ground layer was a 0.813 mm thick Rogers RO4003C copper-clad sheet whose relative permittivity $\varepsilon_{r2} = 3.55$ and loss tangent $\tan\delta = 0.0027$. The conformal metasurface was fabricated on the flexible substrate, DuPont AP 8525R, with a thickness of 0.0508 mm, a relative permittivity of $\varepsilon_{r3} = 3.4$, and a loss tangent $\tan\delta = 0.004$. The overall size of the assembled system was 22 mm × 22 mm × 15 mm ($0.27\lambda \times 0.27\lambda \times 0.19\lambda$, where λ is the free-space wavelength at the center frequency of the LB, 3.7 GHz).

Fig. 23 shows the simulated and measured S-parameters. The measurement results generally agree well with the simulated ones, despite the measured bandwidths being slightly broader than the simulated results. The latter is due to the additional losses arising from the connectors and coaxial cables. The measured 10-dB impedance bandwidths in the LB and HB are from 3.45 to 3.97 GHz (14.1%) and from 5.82 to 6.53 GHz (11.5%), respectively. The measured transmission coefficients between port1 and port2 are below -20 dB across both the LB and HB.

The far-field radiation performance measurements were conducted in an anechoic chamber in the Tech Lab, University of Technology Sydney (UTS), Sydney, Australia. A photo of the antenna under test (AUT) is provided in Fig. 22(b). The measured results are given in Fig. 24. The effective descattering frequency range is 3.5–3.9 GHz in the LB and 6.0–6.4 GHz in the HB despite the impedance bandwidths being slightly wider. The measured and simulated radiation patterns closely align, exhibiting consistent boresight patterns across all sampled frequencies. Nevertheless, the measured cross-polarization levels, especially in the *xoz*-plane, were higher than their simulated values. These differences are attributed primarily to practical manufacturing tolerances associated with milling the very hard ceramic. While the simulated antenna structure maintains perfect symmetry with respect to the *xoz*-plane, real-world fabrication introduced subtle imperfections. Assembly flaws, which included slight angle rotations of the ring metasurface, misalignment of the DRAs, and minor irregularities when the SMA connectors and cables were soldered, also increased the unexpected differences from the optimized design. All of these factors contributed to the larger than predicted cross-polarization levels in that plane. Importantly and despite these issues, the measured cross-polarization levels remained quite low, consistently measuring less than -20 dB across all samples. Note that the high backlobe level is attributed mainly to the slot line etched on the ground plane and the microstrip feedlines on the backside of the substrate. Both contribute to the back radiated fields. The addition of another metal layer at the bottom would convert the microstrip lines into strip lines and might help mitigate the undesired back lobe.

Fig. 25 plots the simulated and measured realized gain

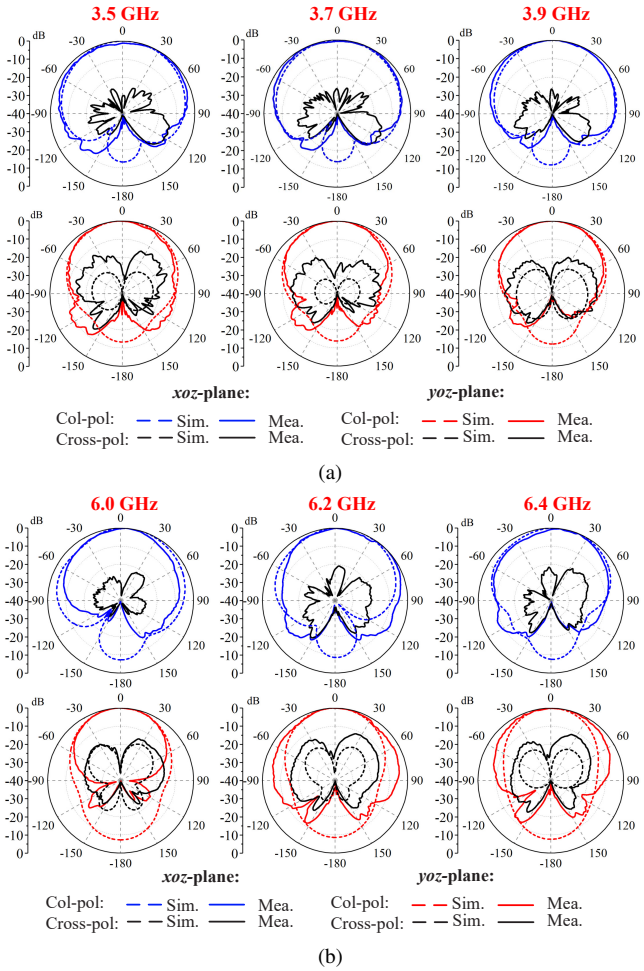

Fig. 24. Simulated and measured radiation patterns of the dual-band shared-aperture DRA. (a) LB. (b) HB.

patterns of the LB and HB elements. The measured realized gains were 4.4–5.5 dBi in the LB and 5.8–6.2 dBi in the HB. Overall, they were only 0.5 dB lower than their simulated values.

The results presented in this section affirm the efficacy of the developed methods for mitigating cross-band interference in a dual-band shared-aperture DRA system. The concept of embedding a smaller DRA, designed for a higher frequency band, within a larger DRA, intended for a lower frequency band, offers significant space-savings. The challenges of substantial cross-band coupling and scattering in this configuration, which diminish the port-to-port isolation and deteriorates the radiation patterns, were overcome with an optimized design based on a semi-transmissive conformal metasurface and a tailored feed structure. The metasurface served to restore the degraded radiation pattern in the HB while preserving the characteristics of the LB radiation patterns. The innovative feed structure featured two C-shaped slots and a long tuning fork feedline. This design was instrumental in reducing coupling, thereby enhancing isolation between the ports that excite the LB and HB DRAs.

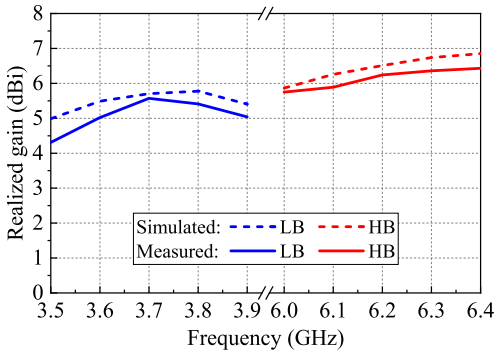

Fig. 25. Simulated and measured realized gains of the dual-band shared-aperture DRA.

V. CONCLUSION

A dual-band shared-aperture DRA was developed in this work. The system effectively integrates two DRAs into a space-saving configuration, each covering the uplink and downlink of the C-band for satellite communications. The challenges posed by cross-band scattering and coupling between these DRAs were addressed with a conformal semi-transmissive metasurface and two mirror-symmetric C-shaped slots excited by a tuning fork feedline. The radiation patterns realized by each DRA separately were recovered, and the isolation between the two bands was enhanced with those innovative elements. These suppression techniques are distinctly different from those cross-band scattering and coupling mitigation methods that have been introduced in metal-based co-located base-station radiating elements. The design process and working principles were discussed in detail, providing valuable insights for future design endeavors. A prototype of the optimized dual-band shared-aperture DRA was fabricated and measured. The simulated and measured impedance and radiated field characteristics demonstrated the efficacy of the developed descattering and decoupling structures. This work presented a promising solution for mitigating cross-band interference in multi-band antenna systems operating within space-constrained environments such as those on UAVs.

VI. ACKNOWLEDGMENT

The authors wish to express their deepest appreciation to Prof. Yong Mei Pan, South China University of Technology, China, for her invaluable assistance in confirming the operating modes of the DRAs in this study.

REFERENCES

[1] P.-Y. Qin, L.-Z. Song, and Y. J. Guo, "Conformal transmitarrays for unmanned aerial vehicles aided 6G networks," *IEEE Commun. Mag.*, vol. 60, no. 1, pp. 14–20, 2022.

[2] L. Leszkowska, M. Rzymowski, K. Nyka, and L. Kulas, "High-gain compact circularly polarized X-band superstrate antenna for CubeSat applications," *IEEE Antennas Wireless Propag. Lett.*, vol. 20, no. 11, pp. 2090–2094, 2021.

[3] Z. Akhter, R. M. Bilal, and A. Shamim, "A dual mode, thin and wideband MIMO antenna system for seamless integration on UAV," *IEEE Open J. Antennas Propag.*, vol. 2, pp. 991–1000, 2021.

[4] S. Zarbakhsh and A. R. Sebak, "Multifunctional drone-based antenna for satellite communication," *IEEE Trans. Antennas and Propag.*, vol. 70, no. 8, pp. 7223–7227, 2022.

[5] X.-Y. Zhang, D. Xue, L.-H. Ye, Y.-M. Pan, and Y. Zhang, "Compact dual-band dual-polarized interleaved two-beam array with stable radiation pattern based on filtering elements," *IEEE Trans. Antennas and Propag.*, vol. 65, no. 9, pp. 4566–4575, 2017.

[6] H.-H. Sun, B. Jones, Y. J. Guo, and Y. H. Lee, "Suppression of cross-band scattering in interleaved dual-band cellular base-station antenna arrays," *IEEE Access*, vol. 8, pp. 222486–222495, 2020.

[7] Y. Liu, S. Wang, N. Li, J.-B. Wang, and J. Zhao, "A compact dual-band dual-polarized antenna with filtering structures for sub-6 GHz base station applications," *IEEE Antennas Wireless Propag. Lett.*, vol. 17, no. 10, pp. 1764–1768, 2018.

[8] X.-H. Ding, J.-Y. Yang, W.-W. Yang, and J.-X. Chen, "Compact dual-band and dual-polarized base station antenna with shared-dipole elements," *IEEE Antennas Wireless Propag. Lett.*, vol. 22, no. 6, pp. 1371–1375, 2023.

[9] Y. Li and Q.-X. Chu, "Coplanar dual-band base station antenna array using concept of cavity-backed antennas," *IEEE Trans. Antennas and Propag.*, vol. 69, no. 11, pp. 7343–7354, 2021.

[10] Y. Chen, J. Zhao, and S. Yang, "A novel stacked antenna configuration and its applications in dual-band shared-aperture base station antenna array designs," *IEEE Trans. Antennas and Propag.*, vol. 67, no. 12, pp. 7234–7241, 2019.

[11] Y. Zhu, Y. Chen, and S. Yang, "Decoupling and low-profile design of dual-band dual-polarized base station antennas using frequency-selective surface," *IEEE Trans. Antennas and Propag.*, vol. 67, no. 8, pp. 5272–5281, 2019.

[12] G.-N. Zhou, B.-H. Sun, Q.-Y. Liang, S.-T. Wu, Y.-H. Yang, and Y.-M. Cai, "Triband dual-polarized shared-aperture antenna for 2G/3G/4G/5G base station applications," *IEEE Trans. Antennas and Propag.*, vol. 69, no. 1, pp. 97–108, 2021.

[13] Y. J. Guo and R. W. Ziolkowski, *Advanced Antenna Array Engineering for 6G and Beyond Wireless Communications*. 1st ed. Hoboken, NJ, USA: Wiley, 2021.

[14] S.-Y. Sun, C. Ding, W. Jiang, and Y. J. Guo, "Simultaneous suppression of cross-band scattering and coupling between closely spaced dual-band dual-polarized antennas," *IEEE Trans. Antennas and Propag.*, vol. 71, no. 8, pp. 6423–6434, 2023.

[15] S. J. Yang, W. Duan, Y. Y. Liu, H. Ye, H. Yang, and X. Y. Zhang, "Compact dual-band base-station antenna using filtering elements," *IEEE Trans. Antennas and Propag.*, vol. 70, no. 8, pp. 7106–7111, 2022.

[16] Y. F. Cao, X. Y. Zhang, and Q. Xue, "Compact shared-aperture dual-band dual-polarized array using filtering slot antenna and dual-function metasurface," *IEEE Trans. Antennas and Propag.*, vol. 70, no. 2, pp. 1120–1131, 2022.

[17] H.-H. Sun, H. Zhu, C. Ding, B. Jones, and Y. J. Guo, "Scattering suppression in a 4G and 5G base station antenna array using spiral chokes," *IEEE Antennas Wireless Propag. Lett.*, vol. 19, no. 10, pp. 1818–1822, 2020.

[18] H.-H. Sun, C. Ding, H. Zhu, B. Jones, and Y. J. Guo, "Suppression of cross-band scattering in multiband antenna arrays," *IEEE Trans. Antennas and Propag.*, vol. 67, no. 4, pp. 2379–2389, 2019.

[19] J. Jiang and Q.-X. Chu, "Dual-band shared-aperture base station antenna array based on 3-D chokes," *IEEE Antennas Wireless Propag. Lett.*, vol. 22, no. 4, pp. 824–828, 2023.

[20] Y. Zhu, Y. Chen, and S. Yang, "Cross-band mutual coupling reduction in dual-band base-station antennas with a novel grid frequency selective surface," *IEEE Trans. Antennas and Propag.*, vol. 69, no. 12, pp. 8991–8996, 2021.

[21] Y. M. Pan, X. Qin, Y. X. Sun, and S. Y. Zheng, "A simple decoupling method for 5G millimeter-wave MIMO dielectric resonator antennas," *IEEE Trans. Antennas and Propag.*, vol. 67, no. 4, pp. 2224–2234, 2019.

[22] H. Xu, Z. Chen, H. Liu, L. Chang, T. Huang, S. Ye, L. Zhang, and C. Du, "Single-fed dual-circularly polarized stacked dielectric resonator antenna for K/Ka-band UAV satellite communications," *IEEE Trans. Veh. Technol.*, vol. 71, no. 4, pp. 4449–4453, 2022.

[23] A. Dadgarpour, B. Zarghooni, B. S. Virdee, T. A. Denidni, and A. A. Kishk, "Mutual coupling reduction in dielectric resonator antennas using metasurface shield for 60-GHz MIMO systems," *IEEE Antennas Wireless Propag. Lett.*, vol. 16, pp. 477–480, 2017.

[24] M. Farahani, J. Pourahmadazar, M. Akbari, M. Nedil, A. R. Sebak, and T. A. Denidni, "Mutual coupling reduction in millimeter-wave MIMO antenna array using a metamaterial polarization-rotator wall," *IEEE Antennas Wireless Propag. Lett.*, vol. 16, pp. 2324–2327, 2017.

[25] M. J. Al-Hasan, T. A. Denidni, and A. R. Sebak, "Millimeter-wave EBG-based aperture-coupled dielectric resonator antenna," *IEEE Trans. Antennas and Propag.*, vol. 61, no. 8, pp. 4354–4357, 2013.

[26] R. Karimian, A. Kesavan, M. Nedil, and T. A. Denidni, "Low-mutual-coupling 60-GHz MIMO antenna system with frequency selective surface wall," *IEEE Antennas Wireless Propag. Lett.*, vol. 16, pp. 373–376, 2017.

[27] Y. Hu, Y. M. Pan, and M. Di Yang, "Circularly polarized MIMO dielectric resonator antenna with reduced mutual coupling," *IEEE Trans. Antennas and Propag.*, vol. 69, no. 7, pp. 3811–3820, 2021.

[28] M. Elahi, A. Altaf, E. Almajali, and J. Yousaf, "Mutual coupling reduction in closely spaced MIMO dielectric resonator antenna in H-plane using closed metallic loop," *IEEE Access*, vol. 10, pp. 71576–71583, 2022.

[29] Y. M. Pan, X. Qin, Y. X. Sun, and S. Y. Zheng, "A simple decoupling method for 5G millimeter-wave MIMO dielectric resonator antennas," *IEEE Trans. Antennas and Propag.*, vol. 67, no. 4, pp. 2224–2234, 2019.

[30] Y. M. Pan, Y. Hu, and S. Y. Zheng, "Design of low mutual coupling dielectric resonator antennas without using extra decoupling element," *IEEE Trans. Antennas and Propag.*, vol. 69, no. 11, pp. 7377–7385, 2021.

[31] X.-F. Wang, L.-L. Yang, X.-Y. Wang, and J.-X. Chen, "Wideband self-decoupling dielectric patch filtennas with stable filtering response," *IEEE Access*, vol. 10, pp. 126561–126568, 2022.

[32] Y.-Z. Liang, F.-C. Chen, W.-F. Zeng, and Q.-X. Chu, "Design of self-decoupling dielectric resonator antenna with shared radiator," *IEEE Trans. Antennas and Propag.*, vol. 71, no. 1, pp. 1053–1058, 2023.

Xing-Yu Cheng (Student Member, IEEE) was born in Shangluo, Shaanxi, China, in 1996. She received her B.Eng. and M.Eng. degrees in Electronic and Communication Engineering from Xidian University, Xi'an, China, in 2018 and 2021, respectively. Currently, she is pursuing her Ph.D. degree with the Global Big Data Technologies Center (GBDTC) at the University of Technology Sydney (UTS) in Sydney, NSW, Australia.

Her current research interests include dielectric resonator antennas, metasurfaces, antenna arrays, satellite communications, and base station antennas.

Can Ding (M'16-SM'24) received a Bachelor Degree in integrated circuit and integrated system from Xidian University, Xi'an, China, in 2009, and a joint Ph.D. Degree from Xidian University and Macquarie University, Australia, in electromagnetic fields and microwave technology in 2016. From 2015 to 2017, he was a Post-Doctoral Research Fellow with the University of Technology Sydney (UTS), Sydney, where he is currently a Senior Lecturer with the School of Electrical and Data Engineering (SEDE), Faculty of Engineering and IT (FEIT), and also a Core Member of the Global Big Data Technologies Center (GBDTC).

His contributions to the antenna and propagation society has been to advance the understanding and the evolution of cutting-edge technologies that are leading to the cost-efficient deployment of 5G networks. Notably, his works have facilitated the management and even elimination of self- and cross-band interference between the 3G/4G/5G antennas in base station systems. These pioneering research efforts have garnered recognition in the form of a prestigious ARC DECRA grant in 2020, Australia's most prestigious grant for early career researchers. His state-of-the-art base station antenna works have occurred in close collaborations with industry and have been successfully translated into solutions for cellular network operators across Australia. His accomplishments encompass several research and industry projects, patented innovations, and a portfolio of over 100 publications in top-tier journals and conferences. He is an IEEE AP-S Young Professional Ambassador in 2024. He serves as an associated editor for IEEE Antennas and Wireless Propagation Letters.

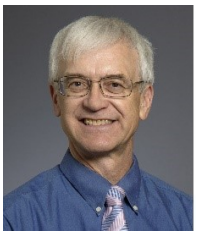

Richard W. Ziolkowski (M'87-SM'91-F'94-LF'20) received (*magna cum laude*) the B. Sc. degree (Hons.) in physics from Brown University, Providence, RI, USA, in 1974; the M.S. and Ph.D. degrees in physics from the University of Illinois at Urbana-Champaign, Urbana, IL, USA, in 1975 and 1980, respectively; and an Honorary Doctorate degree from the Technical University of Denmark, Kongens Lyngby, Denmark in 2012.

He is currently a Professor Emeritus with the Department of Electrical and Computer Engineering at the University of Arizona, Tucson, AZ, USA. He was a Litton Industries John M. Leonis Distinguished Professor in the College of Engineering as well as a Professor in the College of Optical Sciences until his retirement in 2018. He was also a Distinguished Professor in the Global Big Data Technologies Centre in the Faculty of Engineering and Information Technologies (FEIT) at the University of Technology Sydney, Ultimo NSW Australia from 2016 until 2023. He was the Computational Electronics and Electromagnetics Thrust Area Leader with the Engineering Research Division of the Lawrence Livermore National Laboratory before joining The University of Arizona in 1990.

Prof. Ziolkowski was the recipient of the 2019 IEEE Electromagnetics Award (IEEE Technical Field Award). He became a Fellow of OPTICA (previously the Optical Society of America, OSA) in 2006, and a Fellow of the American Physical Society (APS) in 2016. He was the 2014-2015 Fulbright Distinguished Chair in Advanced Science and Technology (sponsored by DSTO, the Australian Defence Science and Technology Organisation). He served as the President of the IEEE Antennas and Propagation Society (AP-S) in 2005 and has had many other AP-S leadership roles. He is also actively involved with the International Union of Radio Science (URSI) and the European Association on Antennas and Propagation (EurAAP) professional societies.